Classical and quantum-mechanical scaling of ionization from excited hydrogen atoms in single-cycle THz pulses

M. Chovancova,[1] H. Agueny,[1] J. J. Rørstad,[2] and J. P. Hansen[1]
[1]*Department of Physics and Technology, Allegt. 55, University of Bergen, N-5007 Bergen, Norway*
[2]*Department of Physics and Astronomy, Aarhus University, 8000 Aarhus C, Denmark*
(Received 19 April 2017; revised manuscript received 12 July 2017; published 25 August 2017)

Excited atoms, or nanotip surfaces, exposed to strong single-cycle terahertz radiation emit electrons with energies strongly dependent on the characteristics of the initial state. Here we consider scaling properties of the ionization probability and electron momenta of H(nd) atoms exposed to a single-cycle pulse of duration 0.5–5 ps, with $n = 9,12,15$. Results from three-dimensional quantum and classical calculations are in good agreement for long pulse lengths, independent of pulse strength. However, differences appear when the two approaches are compared at the most detailed level of density distributions. For the longest pulse lengths a mixed power law, n-scaling relation, $\alpha n^{-4} + (1-\alpha)n^{-3}$ is shown to hold. Our quantum calculations show that the scaling relation puts its imprint on the momentum distribution of the ionized electrons as well: By multiplying the emitted electron momenta of varying initial n level with the appropriate scaling factor the spectra fall onto a common momentum range. Furthermore, the characteristic momenta of emitted electrons from a fixed n level are proportional to the pulse strength of the driving field.

DOI: 10.1103/PhysRevA.96.023423

I. INTRODUCTION

Terahertz (THz) radiation technologies are at present advancing with promising perspectives in a wide range of scientific fields, from fundamental science to real-world applications [1]. Owing to the properties of THz radiation based on low photon energies, the emerging technology has been suggested as a useful source for medical imaging and security [2,3]. In recent years, investigation of single- and half-cycle THz pulses for driving nonlinear phenomena has become possible [4,5], which has exposed new phenomena. For instance, recently, it has been demonstrated experimentally that a strong single-cycle THz pulse applied to excited atoms [6] has led to electron emission with higher energies from tightly bound Rydberg states and with increasing pulse strength. Furthermore, a novel n^{-3} (where n is the quantum number) scaling has been found for the field strength required to attain 10% ionization probability, which later was shown to be valid for arbitrary ionization probability [7]. A similar phenomenon has been discovered for nanosized solid tips exposed to THz pulses: Increasingly narrow tips result in a spectrum of increasingly fast electrons [8]. Studies of the response of solid-state systems to THz radiation is in its infancy. In this context it is relevant to understand the detailed nature of the single atom response to THz radiation in order to separate potential collective phenomena from single atom effects.

On the theoretical side, for single-atom interactions, an empirical scaling relation for 10% ionization probability was put forward by Yang and Robichaux [9], which was shown to be valid for a wide pulse strength and duration range. It gives n^{-4} scaling for pulse durations larger than the classical orbit period of the Rydberg atom (T_n) and a n^2 scaling behavior for short pulses. In that work the quantum calculations are restricted to the initial $n = 15$, $l = 2$ states only while classical trajectory Monte Carlo (CTMC) calculations are the basis of the majority of their work. The dynamics of electron ionization from $n = 15$ levels was further considered in great detail based on time-dependent Schrödinger equation (TDSE) and CTMC calculations in parallel [10]. Here they found excellent agreement between the two approaches and showed that electron emission is strongly favoured along an axis pointing in the opposite direction of the electric polarization vector in the second half-cycle of the pulse. None of these calculations were compared directly with the experimental results of Ref. [6].

In this work we therefore analyze the degree of scaling of the ionization of hydrogen for arbitrary ionization probability from the initial $n = 9,12,15$ d states based on a full three-dimensional (3D) solution of the TDSE and CTMC method. We compare the results for pulses with various strengths and durations. In particular, we compare our results directly with the calculations in [10] and to the experiment in [6]. Furthermore, we explore the characteristics of the emitted electrons for different field ionization. We arrive at three main conclusions and results: First, the 3D quantum calculations, which are in agreement with Ref. [10], support a different scaling than the experimental results of Ref. [6]. Second, even though our CTMC and TDSE results in general agree well at the total probability level, clear discrepancies appear when the two methods are compared at the differential level. In Ref. [10] almost perfect agreement was reported for kinetic emission in the forward or backward direction. Third, we show that application of scaling to the momenta of the emitted electrons puts the spectra on almost the same momentum range. In the next section we describe the applied numerical procedures. Then we present and discuss the main results. Finally, concluding remarks are provided in the last section. Atomic units are used throughout unless otherwise stated.

II. THEORETICAL MODEL

A. TDSE

Within the semiclassical (strong-field) approximation we solve the TDSE,

$$\left[H_e(\vec{r},t) - i\frac{\partial}{\partial t}\right]\psi(\vec{r},t) = 0, \tag{1}$$

where the electronic Hamiltonian contains the field-free Hamiltonian and the time-dependent interaction part given in the length gauge with electric field along the z direction, $\vec{E}(t) = E(t)\vec{e}_z$. To validate the results we first compare with the results in [10] where an exponential expression was used for the electric field,

$$E(t) = -\frac{E_0 C_0 t}{t_w} \exp\left[-\left(\frac{t}{t_w}\right)^2 - 0.1\left(\frac{t}{t_w}\right)^4\right]. \quad (2)$$

Here E_0 is the maximum pulse strength, and C_0, t_w are constants given in [10]. The remaining calculations are performed with a much simpler expression for the electric field,

$$E(t) = \begin{cases} -E_0 \sin(\omega t) & \text{if } -T < t < 0 \\ -E_0 \beta \sin(\beta\omega t) & \text{if } T/\beta > t > 0 \\ 0 & \text{otherwise,} \end{cases} \quad (3)$$

with $\beta \sim 1.5$. This equation grasps the main feature of a single-cycle THz pulse related to the experiments [6,8]; a first positive half-cycle of duration T and a shorter negative and more intense half-cycle of duration T/β. The pulse strength refers to the maximum value of the electric field, i.e., $E_0(n) = E_0\beta$, where n refers to the initial principal quantum number. There are two additional technical advantages of the field expressed by Eq. (3) as well: It can be integrated giving simple analytical expressions for the vector field $A = -\int E(t')dt'$ and the free-field displacement $\alpha = -\int A(t')dt'$. Secondly, the pulse has a well defined start $(-T)$ and end time (T/β). We obtain very similar results for the fields of Eqs. (3) and (2) for $\beta = 1$, but with a factor of 2 shorter simulation time.

Two major numerical challenges with strong THz pulses are related to the long integration times in addition to the required sizes of the numerical grids. Even if techniques have been developed to calculate differential quantities in special situations [11], the full wave function in general needs to be kept on the grid to allow for extraction of all measurable quantities accurately. In the present case at the strongest pulse strength, for example, the wave function initially propagates along the negative z axis and opposite in the final half-cycle. If the grid size is too small, a part of the wave function is absorbed in the first half-cycle and by that the dynamics in the second phase of the field becomes restricted.

The TDSE is integrated using the split-step Fleck-Hermann method [12]. The initial (hydrogen) Rydberg states considered throughout the investigation are analytically known. When put on the grid they are completely stable in absence of electric fields. Here, we need only to consider states with the $m = 0$ component of the magnetic quantum number due to the field polarization. The time-dependent wave function is then expanded in spherical harmonics in the θ and r coordinates as

$$\Psi(r_i,\theta_j,t) = \sum_{l=0}^{L_{\max}} f_l(r_i,t) Y_{l,0}(\hat{r}_j), \quad (4)$$

where $\hat{r}_j = \theta_j$. For general polarizations the sum runs over m-quantum numbers as well and the present formalism is perfectly valid in that case [13]. Then $\hat{r}$ describes the two spherical angles, $d\hat{r}$ describes integration over both and we keep this more general notation in the following. We track the wave function up to radii up to $r_{\max}$ from where an absorbing mask prohibits reflections. Numerical parameters applied $(r_{\max}, \Delta r, L_{\max}, \Delta t)$ are given in the figure captions. Once the time-dependent wave function is determined, on a sufficiently large grid containing the entire density, the wave function in momentum space is calculated using the same basis of spherical harmonics as in Eq. (4). We define the Fourier transform

$$\langle p|\Psi\rangle = \tilde{\Psi}(\vec{p},t) = \int d^3r\, e^{-i\vec{p}\cdot\vec{r}} \Psi(\vec{r},t) \quad (5)$$

and the plane wave expansion

$$e^{i\vec{p}\cdot\vec{r}} = 4\pi \sum_{L,M=0}^{\infty} i^L j_L(pr) Y^*_{L,M}(\hat{r}) Y_{L,M}(\hat{p}). \quad (6)$$

Here $\hat{r}, \hat{p}$ denotes the spherical angles and $j_L(x)$ is defined by the spherical Bessel function, $J_n(x)$, $j_l(x) = \frac{1}{\sqrt{x}} J_{l+0.5}(x)$. Inserting this expansion into the Fourier transform we find that the radial expansion of Eq. (4) can be expressed in momentum space as

$$\tilde{\Psi}(\vec{p},t) = \sum_{l=0}^{L_{\max}} \tilde{f}_l(p,t) Y_{l,0}(\hat{p}). \quad (7)$$

After the pulse, the continuum part of $\tilde{\Psi}$ spans the basis describing ionization, $\tilde{\Psi}^c(\vec{r},t) = \tilde{\Psi} - \tilde{\Psi}^{\text{bound}}$,

$$\tilde{\Psi}^c(\vec{p},t) = \sum_{l=0}^{L_{\max}} \tilde{f}^c_l(p,t_f) Y_{l,0}(\hat{p}). \quad (8)$$

The momentum functions $\tilde{f}^c_l$ become the Fourier transform of the continuum part of the radial functions. These are obtained by projecting and subtracting all populated hydrogenic bound states at t_f. The differential scattering cross section for emission of an electron with momentum $|p_n|$, integrated over angles, can now be calculated from $\tilde{\Psi}^c$,

$$\frac{d\sigma}{dp_n} = \int d\hat{p}\, p^2 |\langle p|\Psi(\vec{r},t_f)\rangle|^2 = \sum_{l=0}^{L_{\max}} \left|p_n \tilde{f}^c_l(p_n,t_f)\right|^2. \quad (9)$$

The angular resolved cross section requires additional multiplication of phases connected to the long-range property of the Coulomb potential. To achieve the correct expression it is convenient to start from a conventional basis state expansion of the time-dependent wave function,

$$\Psi(\vec{r},t_f) = \sum_m a_m(t_f)\Phi_m(\vec{r}) + \sum_n b_n(t_f)\Phi^c_n(\vec{r}). \quad (10)$$

Here, the sum over $m(n)$ runs over all bound (discretized continuum) states inside a sphere with radius $r_{\max}$. The basis functions are the product of radial and angular states, $\Phi_k(\vec{r}) = \phi_k(r)Y_{l,0}(\hat{r})$, and the grid is assumed to span the entire wave function after the pulse, $1 = \sum_m |a_m(t_f)|^2 + \sum_n |b_n(t_f)|^2$. The connection between the set Ψ_n and the correct outgoing scattering states of the Coulomb problem is obtained when expressing the latter in terms of the discretized basis defined

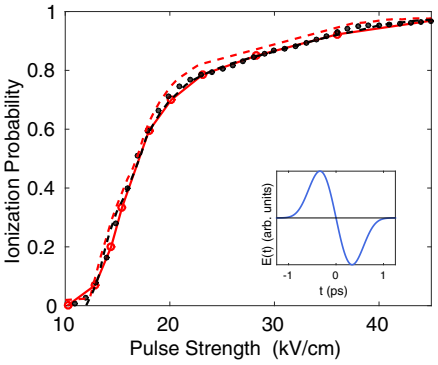

FIG. 1. Ionization probabilities as a function of pulse strength for the symmetric pulse, Eq. (2), sketched in the inset and applied in [10]. The black dashed line is the TDSE results and the dots are the CTMC results from [10]. The red (dark-gray) bulleted curve displays the present TDSE results and the red (dark-gray) dashed line the CTMC results. Parameters for the TDSE computations: $r_{\max} = 4000$, $\Delta r = 0.2441$, $L_{\max} = 128$, $\Delta t = 0.05$ and pulse parameters: $t_w = 2.067\,069 \times 10^4$, $C_0 = 2.385\,525\,5$.

above,

$$\Psi_C(\vec{r}) = \frac{1}{p}\sum_{l=0}^{\infty}\sum_{n} i^l e^{i\delta_l}\phi^c_{n,l}(r;p_n)Y^*_{l,0}(\hat{p})Y_{l,0}(\hat{r}), \qquad (11)$$

where the Coulomb phase shift is $\delta_l = \arg[\Gamma(l+1+i/p)]$ [14]. The projection of the numerical basis of Eq. (10) then becomes

$$\langle\Psi_C|\Psi\rangle = \frac{1}{p}\sum_{l=0}^{L_{\max}}\sum_{n}(-i)^l e^{-i\delta_l} b_n(t_f)Y_{l,0}(\hat{p}). \qquad (12)$$

The differential angular cross section for emission of an electron with any energy in the direction $d\hat{p}$ then becomes

$$\frac{d\sigma}{d\hat{p}} = \int dp\, p^2 |\langle\Psi_C|\Psi\rangle|^2 = \sum_n \left|\sum_{l=0}^{L_{\max}}(-i)^l e^{-i\delta_l} b_n(t_f)Y_{l,0}(\hat{p})\right|^2. \qquad (13)$$

Note that amplitudes of the numerical simulation have to be augmented by the Coulombic phase factors before integration. The same procedure must be carried through for the grid expansion of Eq. (4). Starting again with the projection on the Coulomb functions,

$$\langle\Psi_C|\Psi\rangle = \int d^3r \langle\tilde{\Psi}_C|\vec{r}\rangle\langle\vec{r}|\Psi\rangle = \sum_{l=0}^{L_{\max}}(-i)^l e^{-i\delta_l}\tilde{f}^C_l(p)Y_{l,0}(\hat{p}). \qquad (14)$$

By comparing this expression with Eq. (8) we identify $\tilde{f}^C_l(p) = \tilde{f}^c_l(p)$ and we note that Coulomb phase shifts need to be augmented precisely as in the case of eigenstate expansions, Eqs. (13) and (12). The differential cross sections for emission of an electron with momentum p_n along the direction $d\hat{p}$ then

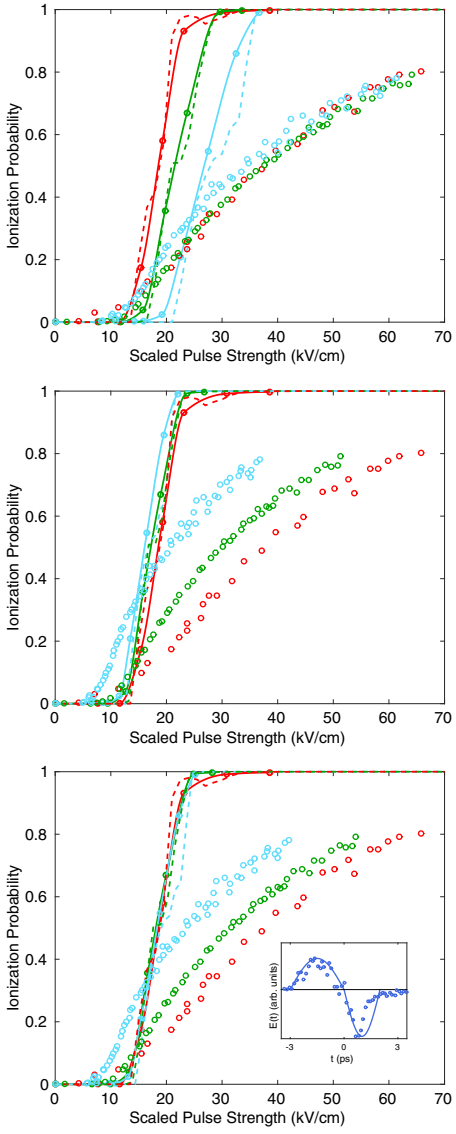

FIG. 2. Ionization probabilities as a function of scaled pulse strength for a pulse shape comparable to the experiment of [6] (cf. inset in the lower panel). Pulse parameters from Eq. (3) are $T = 124\,020$ a.u. ($\omega = 2.533\,13 \times 10^{-5}$ a.u.), $\beta = 1.5$. Probabilities are shown as a function of scaled pulse strength. The upper (middle) panel shows the experimental and computational results based on a n^{-3} (n^{-4}) scaling. The lower panel shows the results for the mixed scaling Eq. (20), with $\alpha = 0.2$. Color coding is according to the initial n state with $n = 15$ as red (dark-gray) lines, $n = 12$ as green (gray) lines, and $n = 9$ as blue (light-gray) lines. Full curves are TDSE results, broken curves are CTMC results, and bullets are experimental data from [6] with the same color coding. Parameters of the TDSE computations: $r_{\max} = 4000$, $\Delta r = 0.2441$, $L_{\max} = 128$, $\Delta t = 0.05$.

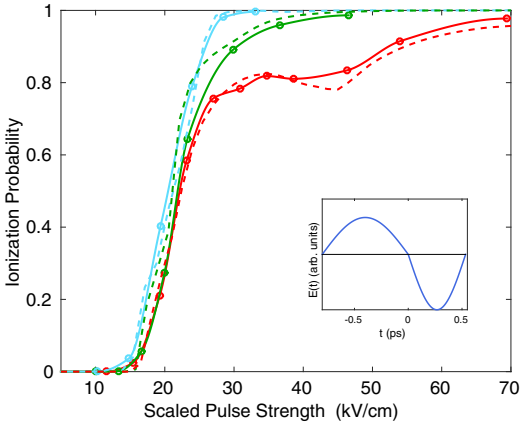

FIG. 3. Ionization probabilities as a function of scaled pulse strength for a pulse shape of Eq. (3), comparable in length to the pulse in Fig. 1. Results are plotted in terms of the mixed scaling Eq. (20), with $\alpha = 0.2$. Pulse parameters are $T = 33\,073.0$ a.u. ($\omega = 9.498\,96 \times 10^{-5}$ a.u.), $\beta = 1.5$. Color coding is according to the initial n state with $n = 15$ as red (dark-gray) lines, $n = 12$ as green (gray) lines, and $n = 9$ as blue (light-gray) lines and full curves are TDSE results. Parameters of the TDSE computations: $r_{\max} = 4000$, $\Delta r = 0.2441$, $L_{\max} = 128$, $\Delta t = 0.05$.

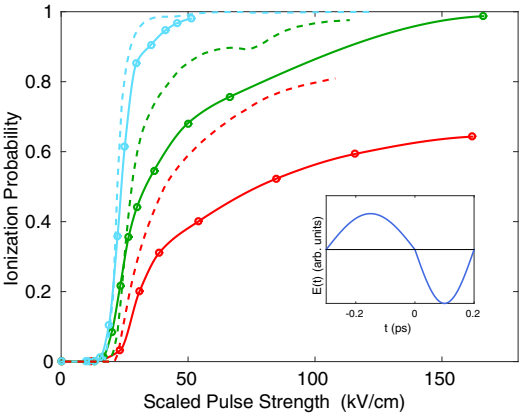

FIG. 4. Ionization probabilities as a function of scaled pulse strength, Eq. (20), for a pulse shape of Eq. (3), with duration only 10% of the pulse in Fig. 2, $T = 12\,402.0$ a.u. ($\omega = 2.533\,13 \times 10^{-4}$ a.u.), $\beta = 1.5$. Color coding is according to the initial n state with $n = 15$ as red (dark-gray) lines, $n = 12$ as green (gray) lines, and $n = 9$ as blue (light-gray) lines and full curves are TDSE results. Parameters of the TDSE computations: $r_{\max} = 4000$, $\Delta r = 0.2441$, $L_{\max} = 128$, $\Delta t = 0.05$.

becomes

$$\frac{d\sigma}{dp_n d\hat{p}} = p_n^2 |\langle \Psi_C | \Psi \rangle|^2 = \left| \sum_{l=0}^{L_{\max}} (-i)^l e^{-i\delta_l} p_n \tilde{f}_l^c(p_n, t_f) Y_{l,0}(\hat{p}) \right|^2 . \quad (15)$$

Thus, the differential cross sections can be computed directly based on the available radial (momentum) basis $f_l^c(r)$ [$\tilde{f}_l^c(p)$] without explicit knowledge of the continuum basis function ϕ_n of Eq. (12). For ionization from the $n = 15$ initial state the final lowest electron momenta are relatively small, in fact of similar magnitude as the strength of the potential energy. Therefore the quantum angular scattering can be affected by the Coulomb phase shifts as well. The differential cross section for electron emission in the forward direction is obtained by integrating over angles corresponding to a positive [$\theta \in (0, \pi/2)$] or negative [$\theta \in (\pi/2, \pi]$] p_z momentum component,

$$\frac{dP^{\text{forward}}}{dp_n} = \int_0^{\pi/2} \int_0^{2\pi} d\hat{p} \frac{d\sigma}{dp_n d\hat{p}}, \qquad \frac{dP^{\text{backward}}}{dp_n} = \int_{\pi/2}^{\pi} \int_0^{2\pi} d\hat{p} \frac{d\sigma}{dp_n d\hat{p}}. \quad (16)$$

These quantities will be discussed at the end of the next section and compared with (phase-free) classical scattering.

B. CTMC

In the CTMC method, Newton's equations are propagated for a large number of the initial conditions describing some main characteristics of an initial quantum probability density. This approach has been applied for decades within heavy particle collisions [15,16] before it was adopted in the study of atoms interacting with strong laser fields [17,18]. A variety of possibilities exist to select the initial distributions [19]. When ionization via tunneling is important an initial distribution of the initial electron position and momenta after tunneling is useful [20]. After propagating the electron positions and momenta according to a given time-dependent interaction, quantum phases may even be added in the final statistics [21].

The basic (standard) CTMC method which we will apply here is based on the selection of initial states which have a fixed energy identical to the initial quantum state in question. The simplest assumption that otherwise the probability density is a constant D is then in N-dimensional space,

$$D d^N r d^N p \delta[E(\vec{r}, \vec{p}) - E_0]. \quad (17)$$

This is referred to as the microcanonical distribution [22], which is based on the formal similarity with the concept of the microcanonical ensemble in statistical physics. There is no proof that this method should model well the quantum probability densities and the field-induced dynamics other than the results. And indeed, fine details related to differential quantities often display discrepancies with full quantum treatments [17,23].

In this approach the energy delta function limits the $2N$-dimensional space to $2N - 1$ dimensions, with the necessity to find the $2N - 1$ uniformly distributed variables. In 3D ($N = 3$) space with two sets of spherical coordinates, the four angles are treated in the standard way of covering uniformly the two spheres in r and p. The remaining radial r and p must be described by only one uniformly distributed variable usually denoted w. This is obtained by transforming $p^2 dp r^2 dr \longrightarrow dE dw$ and $pdp \rightarrow \mu dE$ so that the energy delta function can

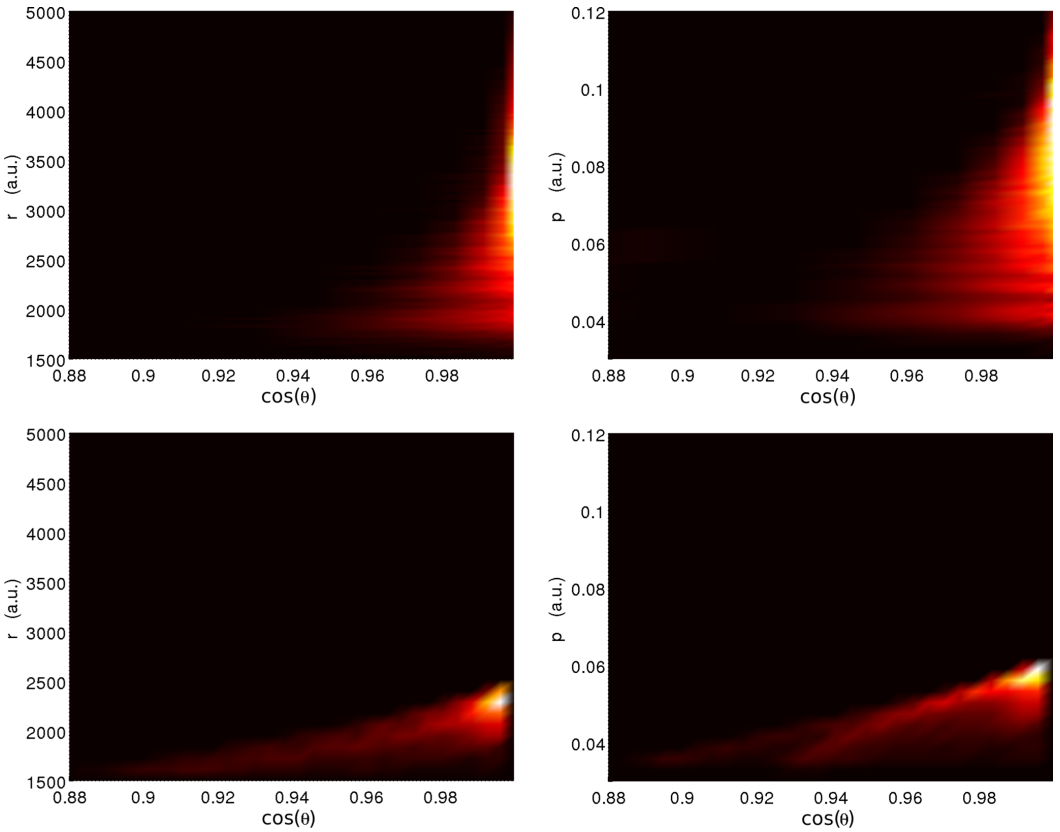

FIG. 5. Probability density distributions at the end of the pulse of the continuum part of the quantum wave function in position space, $|\Psi^c[r, \cos(\theta), t_f]|^2$ (upper left) and momentum space $|\tilde{\Psi}^c[p, \cos(\theta_p), t_f]|^2$ (upper right) for an initial $15d$ state with a pulse strength corresponding to 20% ionization probability ($E_0 = 18$ kV/cm) in Fig. 3. The lower panels show the corresponding densities from CTMC calculations. Pulse parameters from Eq. (3) are as in Fig. 2: $T = 124\,020$ a.u. ($\omega = 2.533\,13 \times 10^{-5}$ a.u.), $\beta = 1.5$. Parameters of the TDSE computations: $r_{\max} = 16\,000$, $\Delta r = 0.2441$, $L_{\max} = 128$, $\Delta t = 0.05$.

be integrated over dE. The variable w can then be found from these requirements.

$$w(r) = \mu \int_0^r p(r')^{\prime 2} dr' = \mu \int_0^r \sqrt{2\mu[E_0 - V(r')]}\, r'^2 dr'. \tag{18}$$

In this equation E_0 is the fixed initial energy and μ is the reduced mass. For more details, see Ref. [22].

In addition, to mimicking the initial $Y_{l=2,m=0}$ character of the quantum initial state, we select only classical initial conditions with angular momentum l, $1.5 < l < 2.5$, and $|l_z| < 0.5$. No sensitivity on the results to other limits for $l \sim 2$, $l_z \sim 0$ is found. Newton's equations are then propagated with up to 500 000 initial states using the adaptive integration method of Shampine and Gordon [24] and carefully checked by the ODE45 routine in MATLAB. In both cases an absolute (relative) error tolerance below 10^{-7} (10^{-9}) has been applied.

III. RESULTS AND DISCUSSION

In the remainder of this paper, scaling laws will be discussed in connection with the ionization probabilities and their momentum distributions from TDSE and CTMC calculations. The angular distributions, which show distinct differences, will be additionally discussed at the end.

We start out by comparing the results of our methods with the results of Ref. [10]. Here, we restrict ourselves to the ionization probabilities as a function of the peak field for the hydrogen $15d$ state, but test calculations with the initial $15s$ show the same degree of agreement. The quantum probabilities are computed by subtracting from unity all bound-state probabilities pertaining to a sphere of a given radius (see Fig. 1 caption). The classical probabilities are obtained by the fraction of final states with positive energy after the pulse and the results from both approaches are plotted in Fig. 1. In the same figure the quantum and classical probabilities of [10] are shown. Results are shown for a

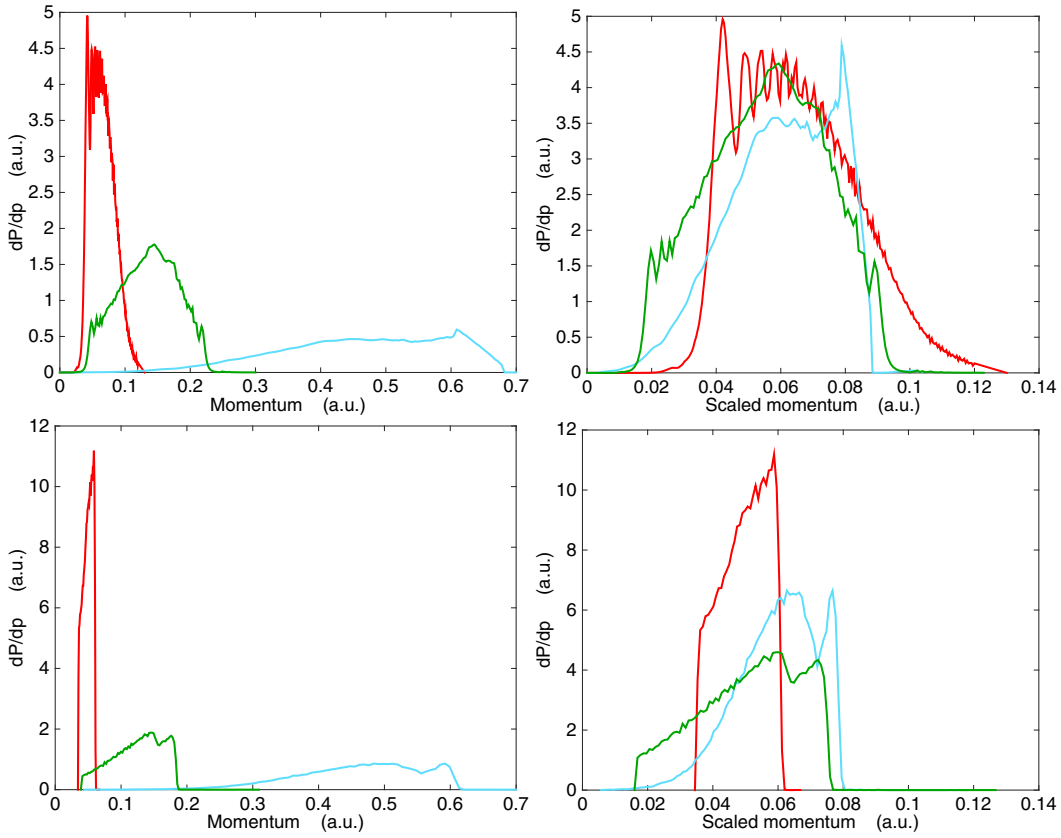

FIG. 6. Momentum distributions of the ionized electron based on the TDSE approach (upper) Eq. (9) and CTMC (lower), for initial states nd with $n = 15$ as red curves (dark-gray), $n = 12$ as green curves (gray), and $n = 9$ as blue (light-gray) curves and for pulse strengths leading to 20% ionization probability from each initial n state ($E_0 = 18$ kV/cm for initial $n = 15$, $E_0 = 36$ kV/cm for initial $n = 12$, $E_0 = 104$ kV/cm for initial $n = 9$). The right column shows the same distributions except that the $n = 12$ and $n = 9$ momentum distributions have been scaled according to the mixed scaling relation, Eq. (20), with $\alpha = 0.2$. Pulse parameters from Eq. (3) are as in Fig. 2: $T = 124\,020$ a.u. ($\omega = 2.533\,13 \times 10^{-5}$ a.u.), $\beta = 1.5$. Parameters of the TDSE computations: $r_{\max} = 16\,000$ ($r_{\max} = 32\,000$ for $n = 9$), $\Delta r = 0.2441$, $L_{\max} = 128$, $\Delta t = 0.05$. The CTMC results are based on 500 000 initial states.

symmetric pulse with a duration of $\sim$2 ps, and its form is illustrated in the inset of the Fig. 1. One can see that the present computed TDSEs are in excellent agreement with those reported in Ref. [10]. Our classical calculations (red dashed lines) very slightly overestimate the ones obtained in [10], possibly a result of different strategies to sample the initial conditions.

In [9] an empirical scaling law was shown to be valid for total ionization (at 10% ionization probability) for a large parameter range of initial states, pulse lengths, and strengths. This was based predominantly on classical calculations but included also results from a few quantum calculations. This scaling law implies a n^2 scaling behavior for pulse durations shorter than the classical orbit period of the Rydberg atom ($T_n \sim n^3$). At long pulse lengths, their scaling law reproduces the results of the classical over the barrier model, i.e., a n^{-4} scaling. In the transition region between these two extrema any kind of power/nonpower laws may occur, including the measured and reported n^{-3} scaling in [6].

Instead of testing scaling law in [9] for computations with different initial levels and probabilities, we here aim to investigate the possible degree of scaling at all ionization probabilities for selected single-cycle pulses. We will consider pulse lengths comparable to the $n = 15$ orbit time of $\sim$0.5 fs, and upward to $\sim$5 fs, the experimental pulse length in [6]. In Fig. 2 we compare our calculated results with the experimental results directly and for various forms of scaling. In the upper panel the experimental ionization probabilities of the initial $n = 9, 12, 15$ states are shown on a common scaled axis defined by $(n/15)^3$ [7]. We observe that this scaling is excellent for the experimental results but rather poor for the calculations. On the other hand, TDSE and CTMC probabilities are in

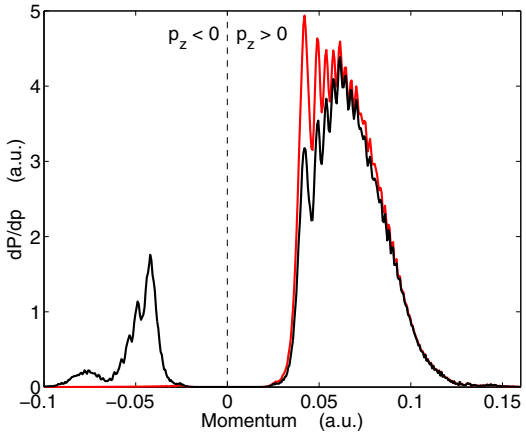

FIG. 7. Forward and backward quantum differential momentum emission probability (black curve) for the initial state $n = 15d$, $E_0 = 18$ kV/cm, Eq. (16), and compared to the momentum distribution of Eq. (9), the red (dark-gray) curve shown in Fig. 6. Parameters of the TDSE computations: $r_{\max} = 16\,000$, $\Delta r = 0.2441$, $L_{\max} = 128$, $\Delta t = 0.05$.

good agreement. The situation switches by applying over the barrier scaling, $(n/15)^4$ in the middle panel of Fig. 2. Now the calculations shows a higher degree of scaling while the scaling of the experimental results are poor.

A dynamical classical mechanism behind the observed n^{-3} scaling was put forward in Ref. [6]. Interestingly, a one-dimensional quantum tunneling mechanism provides the same power-law dependence independent of field strength [25]. In 3D, the weak-field adiabatic tunneling theory provides a leading exponential term which partly scales as n^{-3} as well [26]. Thus, tunneling offers a quantum-mechanical mechanism leading to the observed scaling. The strong external field does, however, open for over the barrier ionization as well. When the two processes takes place at the same time a combination of n^{-3} and n^{-4} scaling may show up in the results. A mixed power-law scaling factor would then emerge on the form

$$E_0^{sf}(n) = \alpha n^{-4} + (1-\alpha)n^{-3}, \tag{19}$$

where the parameter $0 \geqslant \alpha \leqslant 1$. Given an ionization probability for a reference n level, say $n = 15$, the scaled pulse strength of ionization from other n levels at a given real pulse strength $E_0(n)$ becomes

$$E_0^{\text{scaled}}(n) = \frac{E_0^{sf}(n)}{E_0^{sf}(n=15)} E_0(n). \tag{20}$$

If the present scaling is universally valid the ionization probability for varying initial n levels falls on the same curve for a fixed value of the parameter α. In the lower panel of Fig. 2 it is interesting to observe that the computed quantum ionization probabilities exhibit this property for $\alpha = 0.2$. Even the CTMC calculations display the same scaling property for ionization probabilities below 50%. However, putting the experimental results through this scaling procedure only slightly improves the situation from the middle panel of Fig. 2. A potential origin of the discrepancy might be related to the fact that the experiment is performed with Na atoms and the calculations are with H atom(s). However, the quantum defects of the initial nd states in Na are very small and a complete change of scaling is hardly expected between the two atomic systems [9]. Given the agreement with independent calculations we can only conclude that we here document an unresolved discrepancy between theory and experiment which calls for an iteration or independent work on the experimental and possibly also on the computational side.

In Fig. 3 we show our results for a shorter pulse length than the one in Fig. 2, and comparable to the one in Fig. 1. In relation to Fig. 2 the time-dependent field now has a stronger (negative) pulse strength in the second half-cycle as compared to the first. We again note a sharp rise in the ionization probability at the same pulse strength range as in Figs. 1 and 2 and that the scaling procedure as outlined above works very well up to an ionization probability around 70%. At that point the $n = 15$ ionization probability flattens out and oscillates, a mechanism discussed in [6]. It occurs when the pulse length becomes comparable to the classical orbit time, $T_n \propto n^3$. The results of a much shorter pulse duration ($\sim$0.5 ps) are shown in Fig. 4. At this point the scaling procedure is only valid at smallest ionization probabilities. At ionization probabilities exceeding 10% the results of classical and quantum calculations disagree. This indicates that the empirical scaling relation put forward in [9] is limited to small ionization probabilities only.

In the remaining part of this section we will study the momentum distributions in more detail. It generally requires much more computationally expensive calculations as the entire wave function needs to be kept on the grid until the electric field vanishes. The momentum and angular distributions indeed provide a deeper understanding of the ionization dynamics. In this context, it was found in the recent experiment [6], by measuring the electron energy distributions for different n states, that lower initial n gives generally higher energies of the emitted electrons. We address here two main questions: First, to which degree does the mixed scaling law of Eq. (19) imprint itself on the spectrum of emitted electrons? Second, to which extent do the CTMC and TDSE calculations agree when the differential distribution is studied in detail?

The starting point amounts to examining the ionization dynamics in the two-dimensional position and momentum spaces at the end of the laser pulse. Figure 5 shows the spatial distribution of the continuum part of the electron-probability density (left panels) and the corresponding momentum distribution (right panels) for the initial $15d$ state at 20% ionization probability (see caption for further details). The distributions are quantum (upper panels) and classical (lower panels) and they are seen to display great differences. The spreading, the mean position, and momentum of the outgoing distribution differ. With a less detailed focus there are also common features: It is seen that the electron density which is nonzero along a limited range of $(r, \cos\theta)$ values corresponds to ionized electrons propagating along the positive z axis and are centered at positive z values immediately after the pulse. This is consistent with the ionization dynamics taking part predominantly in the final half-cycle of the pulse. In the quantum results, we also observe the emergence of oscillatory

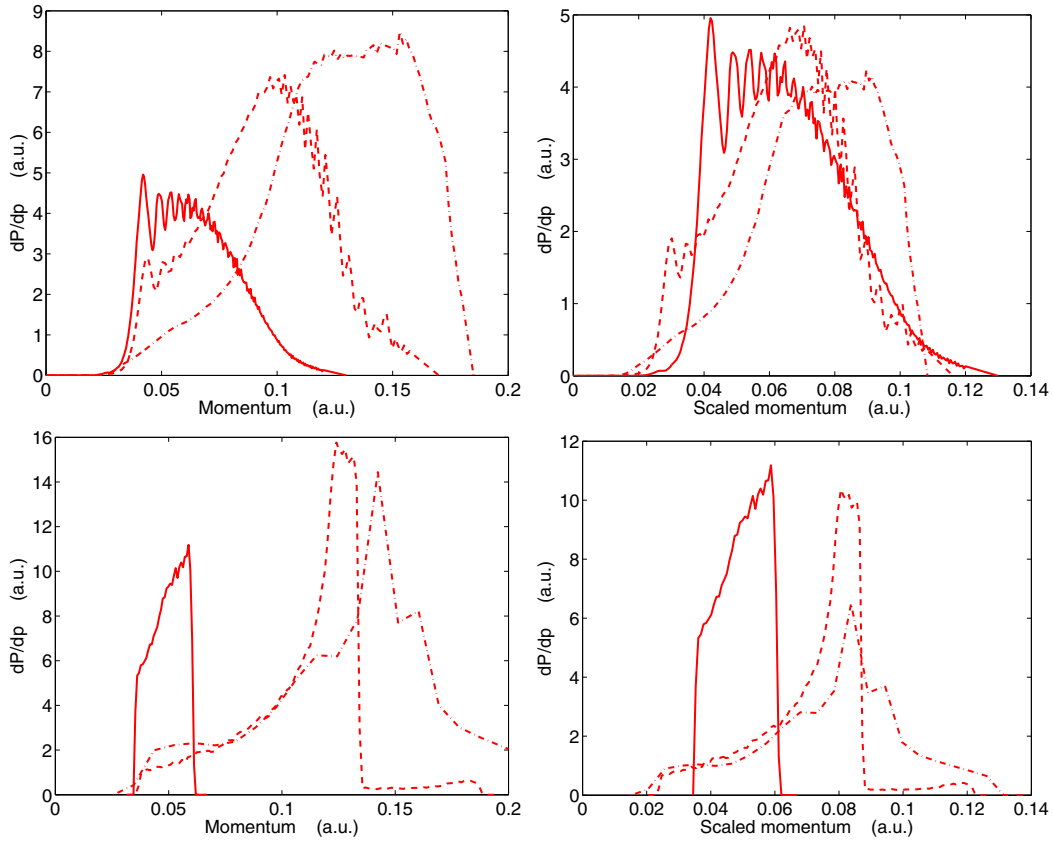

FIG. 8. Upper panels: Momentum distributions from the initial $n = 15d$ state for for three different pulse strengths $E_0 = 15.8$ kV/cm (full line), $E_0 = 18.5$ kV/cm (dashed line), and $E_0 = 21.6$ kV/cm (dashed-dotted line). Pulse parameters from Eq. (3) are as in Fig. 2: $T = 124\,020$ a.u. ($\omega = 2.533\,13 \times 10^{-5}$ a.u.), $\beta = 1.5$. The pulse strengths give ionization probabilities of 20%, 50%, and 73% for the TDSE calculations. The upper right panel shows the distribution with a linearly scaled momenta [cf. Eq. (22)] and normalized to an ionization probability of 20%. Lower panels: Corresponding spectra based on CTMC calculations with 500 000 initial states. Parameters of the TDSE computations: $r_{\max} = 16\,000$, $\Delta r = 0.2441$, $L_{\max} = 128$, $\Delta t = 0.05$.

wavelike structures which do not appear in classical results. A related phenomenon has been discussed previously in Refs. [27] in a multicycle extreme-ultraviolet pulse, and in studies of strong-field few-cycle ionization of the ground state about 20 years ago [17,28].

We turn now to discuss the scaling properties in connection with the momentum distributions of the ionized electrons. In Fig. 6 we have integrated the distributions over all angles and obtained the differential momentum distribution, dP/dp. In the left panel of Fig. 6 we show the unscaled quantum (upper panels) and classical (lower panels) distributions for three initial $n = 9, 12, 15$ states all at $\sim 20\%$ ionization probability. The general features of quantum distributions are reflected in the classical distributions. These are mainly manifested by a wider distribution describing higher electron momenta for decreasing n. By applying the mixed scaling relation, Eq. (19), to the final state momenta, one can now see that the quantum distributions of all three initial states fall into a common range. To some extent the classical distributions also exhibit this property, but here the scaled range is "less common," as shown in the right column of Fig. 6. This result is consistent with the release of the electron at a narrow range of critical pulse strengths, from which it essentially propagates with little influence of the binding potential, as discussed in [7,9].

The instantaneous CTMC distribution of Fig. 6 does not change at all by letting the particles propagate an additionally long time in the presence of the Coulumb potential only. For the quantum distribution it is not so: The low-energy part of the continuum waves, in particular, may be altered by the Coulomb potential. Thus Coulomb phases need to to be added when computing the final differential forward or backward emission probability [cf. Eq. (15)]. This is displayed in Fig. 7 for the initial $n = 15d$ results in Figs. 5 and 6. We observe

that indeed the Coulomb potential plays a role and causes the low-energy part of the emitted spectrum to be rescattered in the opposite direction from what is seen in Fig. 5. Thus, the forward-backward scattering asymmetry turns out to be different for TDSE and CTMC calculations as well, notably in disagreement with the results in [10] with other pulse shapes, strengths, and durations.

For completeness, we address in Fig. 8 the nature of the momentum distributions for an initial fixed n level and for different ionization probabilities. The left panel of Fig. 8 shows results at three comparable ionization probabilities for the initial $n = 15d$. Both the quantum distribution (upper panels) and the classical one (lower panels) show increasing momenta with increasing pulse strength. But again, the detailed distribution differs in shape. A possible scaling in this case can be argued for by assuming the ratio between the final momenta and the pulse strength of any ionization probability, $x\%$, is almost constant,

$$\frac{p(20\%)}{E_0(20\%)} = \frac{p(x\%)}{E_0(x\%)}. \tag{21}$$

This suggests a scaling relation of the form

$$p^{\text{scaled}}(x\%) = \gamma \frac{E_0(20\%)}{E_0(x\%)} p(x\%) \tag{22}$$

with $\gamma \sim 1$ as a free fitting parameter may work. The spectra are additionally normalized to the same total area. We observe in Fig. 8 (right panel) that the momentum range of emitted electrons from the quantum results scale reasonably well for $\gamma = 0.8$, while the CTMC results differ much more, both in shape and final scaled momentum range.

IV. CONCLUDING REMARKS

We have considered the response of H($n = 9d, 12d, 15d$) atoms to a single-cycle THz pulse with durations from 0.5 to 5 ps in classical and quantum-mechanical time propagation. A scaling law has been found to be generally valid for any ionization probability and for initial $n = 9, 12, 15$ levels when the pulse length becomes similar to, or longer than, the classical period of the n levels under consideration. We further investigated the scaling behavior in connection with the ionized momentum distribution in the long-pulse regime. The same scaling property was here found to be valid in quantum distributions and to a much lesser degree for the classical approach. The Coulomb phases have been shown to be important in the quantum scattering process as well for the initial $n = 15d$ state. Finally, a near linear response of the characteristic momentum range has been found for ionization from a fixed n state with increasing pulse strength.

Interestingly, these phenomena have a counterpart in THz radiation from nanotips, faster electrons from narrower tips, and a linear response for a fixed tip with increased pulse strength [8]. Further investigations in this direction may lead to new imaging devices where the electron spectrum from a fixed pulse may provide structural information of the tip region itself. Before that it seems important to further investigate the scaling relations validity for single atoms in strong THz fields. This applies to electron emission probabilities at the total as well as at the differential level and to converge on parameter ranges where ionization and scattering from classical and quantum based approaches agree.

ACKNOWLEDGMENTS

The research has been supported by UNINETT Sigma2 AS which manages the national infrastructure for computational science in Norway. Numerical calculations were carried out at the Cray XE6 (Hexagon) supercomputer installation at Parallab at the University of Bergen (UiB).

[1] S. S. Dhillon *et al.*, J. Phys. D: Appl. Phys. **50**, 043001 (2017).
[2] M. Tonouchi, Nat. Photon. **1**, 97 (2007).
[3] J. F. Federici, B. Schulkin, F. Huang, D. Gary, R. Barat, F. Oliveira, and D. Zimdars, Semicond. Sci. Technol. **20**, S266 (2005).
[4] J. L. LaRue, T. Katayama, A. Lindenberg, A. S. Fisher, H. Öström, A. Nilsson, and H. Ogasawara, Phys. Rev. Lett. **115**, 036103 (2015).
[5] K. Kovács, E. Balogh, J. Hebling, V. Tosa, and K. Varjú, Phys. Rev. Lett. **108**, 193903 (2012).
[6] S. Li and R. R. Jones, Phys. Rev. Lett. **112**, 143006 (2014).
[7] H. Agueny, M. Chovancova, J. P. Hansen, and L. Kocbach, J. Phys. B: At., Mol. Opt. Phys. **49**, 245002 (2016).
[8] S. Li and R. R. Jones, Nat. Commun. **7**, 13405 (2016).
[9] B. C. Yang and F. Robicheaux, Phys. Rev. A **90**, 063413 (2014).
[10] B. C. Yang and F. Robicheaux, Phys. Rev. A **91**, 043407 (2015).
[11] L. Tao and A. Scrinzi, New J. Phys. **14**, 013021 (2012).
[12] M. R. Hermann and J. A. Fleck, Jr., Phys. Rev. A **38**, 6000 (1988).
[13] J. P. Hansen, T. Sørevik, and L. B. Madsen, Phys. Rev. A **68**, 031401(R) (2003).
[14] P. G. Burke, *R-Matrix Therory of Atomic Collisions* (Springer Verlag, Berlin, 2011).
[15] N. C. Blais and D. L. Bunker, J. Chem. Phys. **37**, 2713 (1962).
[16] R. Abrines and I. C. Percival, Proc. Phys. Soc. **88**, 861 (1966).
[17] J. P. Hansen, J. Lu, L. B. Madsen, and H. M. Nilsen, Phys. Rev. A **64**, 033418 (2001).
[18] J. S. Cohen, Phys. Rev. A **64**, 043412 (2001).
[19] N. D. Cariatore, S. Otranto, and R. E. Olson, Phys. Rev. A **93**, 066702 (2016).
[20] J.-P. Wang and F. He, Phys. Rev. A **95**, 043420 (2017).
[21] E. A. Solov'ev, Eur. Phys. J. D **65**, 331 (2011).
[22] C. O. Reinhold and C. A. Falcón, Phys. Rev. A **33**, 3859 (1986).

[23] A. Dubois and J. P. Hansen, J. Phys. B: At., Mol. Opt. Phys. **29**, L225 (1996).
[24] L. F. Shampine and M. K. Gordon, *Computer Solution of Ordinary Differential Equations: The Initial Value Problem* (Freeman, San Fransisco, 1975).
[25] R. G. Forbes, J. Appl. Phys. **103**, 114911 (2008).
[26] T. Yamabe, A. Tachibana, and H. J. Silverstone, Phys. Rev. A **16**, 877 (1977).
[27] I. A. Ivanov, A. S. Kheifets, K. Bartschat, J. Emmons, S. M. Buczek, E. V. Gryzlova, and A. N. Grum-Grzhimailo, Phys. Rev. A **90**, 043401 (2014).
[28] E. Cormier and P. Lambropoulos, Eur. Phys. J. D **2**, 15 (1998).